



Multiple-humped fission and fusion barriers of actinide and superheavy elements

G. Royer, C. Bonilla

Laboratoire Subatech, UMR : IN2P3/CNRS-Université-EMN,
4 rue A. Kastler, 44307 Nantes Cedex 03, France
(royer@subatech.in2p3.fr)

Abstract

The energy of a deformed nucleus has been determined within a Generalized Liquid Drop Model taking into account the proximity energy, the microscopic corrections and quasi-molecular shapes. In the potential barrier a third peak exists for actinides when one fragment is close to a magic spherical nucleus while the other one varies from oblate to prolate shapes. The barrier heights and half-lives agree with the experimental data. The different entrance channels leading possibly to superheavy elements are studied as well as their α -decay.

1. Introduction

The fission probability and the angular distribution of the fragments support the hypothesis of hyperdeformed states lodging in a third well in several Th and U isotopes¹⁻². In fusion reactions³⁻⁴ performed to produce superheavy elements, transfer reaction events correspond to decay of semi-equilibrated systems from an external potential pocket.

These fission and fusion barriers have been determined⁵⁻⁶ using compact quasimolecular shapes and a generalized liquid drop model including the proximity energy and the shell effects. In fission the

ellipsoidal deformations of the fragments have been taken into account.

2. Actinide nuclei

The one-body nuclear deformation has been investigated in the compact and creviced shape path (see Fig. 1) while, for the two-body shapes, the coaxial ellipsoidal deformations have been taken into account. The dependence of the potential barriers on the assumed two-body shapes and microscopic corrections is displayed in Fig. 2. The shell effects generate the deformation of the ground state and increase the height of the first peak which appears already macroscopically. The proximity energy flattens the potential energy and will explain with the microscopic effects the formation of a second minimum lodging the superdeformed isomeric states for the heavier nuclei. The transition between one-body and two-body shapes is more sudden when the ellipsoidal deformations are allowed. It corresponds to the passage from a quasi-molecular one-body shape to two touching ellipsoidal fragments. The microscopic energy lowers the second peak, shifts it to an inner position and leads to a third minimum. The heavier fragment is a quasi magic nucleus and remains almost spherical while the non magic fragment was born in an oblate shape. When the distance between mass centers increases the proximity energy keeps close the two tips of the fragments and the lighter one reaches a spherical shape which corresponds to a maximum of the shell energy and to the third peak. Later on, the proximity forces

maintain in contact the fragments and the shape of the smallest one becomes prolate. This third barrier appears only in the asymmetric decay channels and for some specific nuclei.

The theoretical⁶ and experimental^{7,8} energies of the maxima and minima of the potential barriers are compared in table 1. While experimentally an asymmetric mass distribution is obtained, theoretically only the results for the most probable exit path are given. The agreement with the experimental data is quite correct.

Within this asymmetric fission model the decay constant is simply the product of the assault frequency by the barrier penetrability. Our theoretical predictions⁶ of the spontaneous fission half-lives are compared with the experimental data in the table 2. There is a correct agreement on 24 orders of magnitude, except for the lightest U isotopes.

3. Heavy and superheavy elements

The synthesis of very heavy elements has apparently strongly advanced recently using cold³ (Zn on Pb) and warm⁴ (Ca on U, Pu and Cm) fusion reactions. The observed decay mode is the α emission. The analysis of the experimental data is discussed⁹⁻¹⁰.

Potential barriers against fusion via the cold fusion reactions ^{70}Zn and ^{86}Kr on ^{208}Pb and warm fusion reactions ^{48}Ca on ^{238}U and ^{248}Cm are displayed in Figs. 3 and 4. The dashed line corresponds to the pure macroscopic potential energy. The dashed-dotted line incorporates the

shell corrections around the sphere. The solid line is adjusted to reproduce the experimental or estimated Q value.

In the cold fusion reactions a wide potential pocket energy appears at large deformations and the inner peak is the highest for the heaviest systems. In the deep minimum fast fission processes may develop since the neck is formed. The remaining excitation energy of the composite system depends on the pre or post equilibrium nature of the neutron evaporation process.

In the warm fusion reactions, the barrier against reseparation being high and wide the system descends easily toward a quasi-spherical shape but with an excitation energy of more than 30 MeV if one assumes a full relaxation. The emission of several neutrons or even an α particle is energetically possible.

The α decay has been viewed¹¹ as a very asymmetric spontaneous fission within the GLDM and the α decay half-lives may be calculated accurately using the following formulas respectively for the even (Z) – even (N), even-odd, odd-even and odd-odd nuclei :

$$\log_{10}[T_{1/2}(s)] = -25.31 - 1.1629A^{1/6}\sqrt{Z} + \frac{1.5864Z}{\sqrt{Q_\alpha}}$$

$$\log_{10}[T_{1/2}(s)] = -26.65 - 1.0859A^{1/6}\sqrt{Z} + \frac{1.5848Z}{\sqrt{Q_\alpha}}$$

$$\log_{10}[T_{1/2}(s)] = -25.68 - 1.1423A^{1/6}\sqrt{Z} + \frac{1.592Z}{\sqrt{Q_\alpha}}$$

$$\log_{10}[T_{1/2}(s)] = -29.48 - 1.113A^{1/6}\sqrt{Z} + \frac{1.6971Z}{\sqrt{Q_\alpha}}.$$

The table 3 gives the predictions for the superheavy elements. The Q_α values are calculated within the Thomas-Fermi model¹². If such nuclei exist, their half-lives vary from microseconds to some days.

An open question is to know whether at very large deformations the nucleon shells can take form before investigating a peculiar exit channel. The knowledge of the moment of neutron emission is also crucial to determine the nature of the reaction.

4. Conclusion

The potential fission and fusion barriers have been determined within a macromicroscopic energy.

Triple-humped fission barriers appear for actinides and specific decay channels. For the superheavy elements the cold fusion reactions take place in a double-humped path. In the warm fusion reactions, there is no deep double-humped barriers but the system has a very high excitation energy.

References

1. A. Krasznahorkay et al, Phys. Rev. Lett. 80 (1998) 2073.
2. J. Blons, C. Mazur, D. Paya, M. Ribrag and H. Weigmann, Nucl. Phys. A 414 (1984) 1.
3. S. Hofmann et al, Z. Phys. A 354 (1996) 229.
4. Yu. Ts. Oganessian et al, Phys. Rev. C 63 (2000) 011301(R).
5. G. Royer and R.A. Gherghescu, Nucl. Phys. A 699 (2002) 479.

6. G. Royer and C. Bonilla : Key topics in nuclear structure, World Scientific, Paestum, 2004, p 559.
7. S. Björnholm and J.E. Lynn, Rev. Mod. Phys. 52 (1980) 725.
8. C. Wagemans, The nuclear fission process, CRC Press, Boca Raton, 1991.
9. P. Armbruster, Eur. Phys. J. A 7 (2000) 23.
10. W. Loveland et al, Phys. Rev. C 66 (2002) 044617.
11. G. Royer, J. Phys. G 26 (2000) 1149.
12. W.D. Myers and W.J. Swiatecki, Nucl. Phys. A 601 (1996) 141.

Characteristics of the potential barriers for actinides

Table 1. Experimental (e) and theoretical (t) first E_a , second E_b and third E_c peak heights and energies E_3 of the third minimum relatively to the ground state energy (in MeV).

Reaction	E_a (e)	E_a (t)	E_b (e)	E_b (t)	E_3 (t)	E_c (t)
${}^{231}_{90}\text{Th} \rightarrow {}^{132}_{50}\text{Sn} + {}^{99}_{40}\text{Zr}$	-	5.5	6.5	7.1	3.9	6.9
					5.6(e)	6.3(e)
${}^{233}_{90}\text{Th} \rightarrow {}^{132}_{50}\text{Sn} + {}^{101}_{40}\text{Zr}$	-	5.6	6.8	7.0	5.0	7.8
					5.2(e)	6.8(e)
${}^{232}_{92}\text{U} \rightarrow {}^{134}_{52}\text{Te} + {}^{98}_{40}\text{Zr}$	4.9	4.5	5.4	5.0	4.2	5.1
${}^{234}_{92}\text{U} \rightarrow {}^{131}_{50}\text{Sn} + {}^{103}_{42}\text{Mo}$	5.6	5.0	5.5	5.9	3.7	5.6
					3.1(e)	
${}^{235}_{92}\text{U} \rightarrow {}^{131}_{50}\text{Sn} + {}^{104}_{42}\text{Mo}$	5.7	5.7	5.8	6.6	5.4	6.9
${}^{236}_{92}\text{U} \rightarrow {}^{132}_{50}\text{Sn} + {}^{104}_{42}\text{Mo}$	5.6	5.5	5.5	6.2	3.1	4.4
					3.1(e)	
${}^{237}_{92}\text{U} \rightarrow {}^{132}_{50}\text{Sn} + {}^{105}_{42}\text{Mo}$	6.1	6.1	5.9	6.5	3.6	6.2
${}^{238}_{92}\text{U} \rightarrow {}^{132}_{50}\text{Sn} + {}^{106}_{42}\text{Mo}$	5.7	5.5	5.7	5.6	4.1	5.6
${}^{238}_{94}\text{Pu} \rightarrow {}^{130}_{50}\text{Sn} + {}^{108}_{44}\text{Ru}$	5.6	5.2	5.0	4.5	3.2	3.6
${}^{239}_{94}\text{Pu} \rightarrow {}^{130}_{50}\text{Sn} + {}^{109}_{44}\text{Ru}$	6.2	5.8	5.5	5.0	4.1	5.6
${}^{240}_{94}\text{Pu} \rightarrow {}^{130}_{50}\text{Sn} + {}^{110}_{44}\text{Ru}$	5.7	5.3	5.1	4.6	-	-
${}^{241}_{94}\text{Pu} \rightarrow {}^{131}_{50}\text{Sn} + {}^{110}_{44}\text{Ru}$	6.0	6.1	5.5	5.6	5.1	5.5
${}^{243}_{94}\text{Pu} \rightarrow {}^{132}_{50}\text{Sn} + {}^{111}_{44}\text{Ru}$	5.9	6.3	5.4	5.2	3.2	4.6
${}^{242}_{95}\text{Am} \rightarrow {}^{131}_{50}\text{Sn} + {}^{111}_{45}\text{Rh}$	6.5	6.8	5.4	5.7	4.1	5.1
${}^{244}_{95}\text{Am} \rightarrow {}^{132}_{50}\text{Sn} + {}^{112}_{45}\text{Rh}$	6.3	7.0	5.4	5.7	2.4	4.2
${}^{243}_{96}\text{Cm} \rightarrow {}^{130}_{50}\text{Sn} + {}^{113}_{46}\text{Pd}$	6.4	6.0	4.2	4.2	2.4	2.7
${}^{245}_{96}\text{Cm} \rightarrow {}^{130}_{50}\text{Sn} + {}^{115}_{46}\text{Pd}$	6.2	6.0	4.8	3.7	-	-
${}^{248}_{96}\text{Cm} \rightarrow {}^{130}_{50}\text{Sn} + {}^{118}_{46}\text{Pd}$	5.7	5.3	4.6	3.0	-	-
${}^{250}_{97}\text{Bk} \rightarrow {}^{130}_{50}\text{Sn} + {}^{120}_{47}\text{Ag}$	6.1	6.4	4.1	3.7	-	-
${}^{250}_{98}\text{Cf} \rightarrow {}^{125}_{49}\text{In} + {}^{125}_{49}\text{In}$	5.6	4.9	-	1.7	-	-
${}^{256}_{99}\text{Es} \rightarrow {}^{128}_{50}\text{Sn} + {}^{128}_{49}\text{In}$	4.8	5.9	-	2.4	-	-
${}^{255}_{100}\text{Fm} \rightarrow {}^{127}_{51}\text{Sb} + {}^{128}_{49}\text{In}$	5.7	5.5	-	1.9	-	-

Spontaneous fission half-lives of actinides

Table 2. Experimental and theoretical spontaneous fission half-lives of actinide nuclei.

Reaction	$T_{1/2,\text{exp}}(\text{s})$	$T_{1/2,\text{th}}(\text{s})$
${}_{92}^{232}\text{U} \rightarrow {}_{52}^{134}\text{Te} + {}_{40}^{98}\text{Zr}$	2.5×10^{21}	3.6×10^{16}
${}_{92}^{234}\text{U} \rightarrow {}_{50}^{131}\text{Sn} + {}_{42}^{103}\text{Mo}$	4.7×10^{23}	8×10^{19}
${}_{92}^{235}\text{U} \rightarrow {}_{50}^{131}\text{Sn} + {}_{42}^{104}\text{Mo}$	3.1×10^{26}	7.7×10^{23}
${}_{92}^{236}\text{U} \rightarrow {}_{50}^{132}\text{Sn} + {}_{42}^{104}\text{Mo}$	7.8×10^{23}	1.0×10^{22}
${}_{92}^{238}\text{U} \rightarrow {}_{50}^{132}\text{Sn} + {}_{42}^{106}\text{Mo}$	2.6×10^{23}	5.3×10^{22}
${}_{94}^{238}\text{Pu} \rightarrow {}_{50}^{130}\text{Sn} + {}_{44}^{108}\text{Ru}$	1.5×10^{18}	2.6×10^{19}
${}_{94}^{239}\text{Pu} \rightarrow {}_{50}^{130}\text{Sn} + {}_{44}^{109}\text{Ru}$	2.5×10^{23}	4.8×10^{22}
${}_{94}^{240}\text{Pu} \rightarrow {}_{50}^{130}\text{Sn} + {}_{44}^{110}\text{Ru}$	3.7×10^{18}	4.8×10^{19}
${}_{95}^{243}\text{Am} \rightarrow {}_{51}^{133}\text{Sb} + {}_{44}^{110}\text{Ru}$	6.3×10^{21}	1.1×10^{23}
${}_{96}^{243}\text{Cm} \rightarrow {}_{48}^{122}\text{Cd} + {}_{48}^{121}\text{Cd}$	1.7×10^{19}	3×10^{21}
${}_{96}^{245}\text{Cm} \rightarrow {}_{50}^{130}\text{Sn} + {}_{46}^{115}\text{Pd}$	4.4×10^{19}	3×10^{20}
${}_{96}^{248}\text{Cm} \rightarrow {}_{50}^{130}\text{Sn} + {}_{46}^{118}\text{Pd}$	1.3×10^{14}	7.7×10^{15}
${}_{98}^{250}\text{Cf} \rightarrow {}_{55}^{140}\text{Cs} + {}_{43}^{110}\text{Tc}$	5.2×10^{11}	4.9×10^{11}
${}_{98}^{250}\text{Cf} \rightarrow {}_{52}^{132}\text{Te} + {}_{46}^{118}\text{Pd}$	5.2×10^{11}	1.2×10^{10}
${}_{99}^{255}\text{Es} \rightarrow {}_{50}^{128}\text{Sn} + {}_{49}^{127}\text{In}$	8.4×10^{10}	8×10^9
${}_{100}^{256}\text{Fm} \rightarrow {}_{47}^{121}\text{Ag} + {}_{53}^{135}\text{I}$	1.0×10^4	82
${}_{102}^{256}\text{No} \rightarrow {}_{51}^{128}\text{Sb} + {}_{51}^{128}\text{Sb}$	110	0.9×10^{-2}
${}_{102}^{256}\text{No} \rightarrow {}_{46}^{116}\text{Pd} + {}_{56}^{140}\text{Ba}$	110	0.3×10^{-1}

Alpha-decay half-lives of superheavy elements

Table 3. Predicted $\text{Log}_{10}[T_{1/2}(\text{s})]$ for the superheavy elements versus the charge and mass of the mother nucleus and Q_{α} .

120	A	295	296	297	298	299	300	301	302	303
	Q$_{\alpha}$ Log[T]	13.59 -5.75	13.92 -7.17	13.78 -6.15	13.58 -6.57	13.33 -5.32	13.63 -6.71	13.91 -6.45	13.95 -7.34	14.07 -6.78
118	A	292	293	294	295	296	297	298	299	300
	Q$_{\alpha}$ Log[T]	12.59 -5.09	12.49 -4.14	12.51 -4.96	12.42 -4.02	12.52 -5.02	12.34 -3.88	12.73 -5.49	12.87 -5.03	12.94 -5.96
117	A	290	291	292	293	294	295	296	297	298
	Q$_{\alpha}$ Log[T]	12.14 -3.47	11.94 -3.58	11.93 -3.00	11.91 -3.55	11.90 -2.96	11.80 -3.34	11.59 -2.23	11.97 -3.76	12.16 -3.65
116	A	287	288	289	290	291	292	293	294	295
	Q$_{\alpha}$ Log[T]	11.52 -2.52	11.55 -3.35	11.50 -2.51	11.34 -2.89	11.33 -2.14	11.03 -2.16	11.15 -1.74	11.19 -2.60	11.06 -1.55
115	A	285	286	287	288	289	290	291	292	293
	Q$_{\alpha}$ Log[T]	10.55 -0.74	10.45 0.26	10.48 -0.59	10.34 0.54	10.24 0.03	10.15 1.07	9.88 1.03	9.75 2.28	9.69 1.56
114	A	284	285	286	287	288	289	290	291	292
	Q$_{\alpha}$ Log[T]	9.64 1.10	9.55 2.07	9.61 1.16	9.53 2.10	9.39 1.80	9.08 3.49	8.73 3.95	8.66 4.90	8.47 4.85

Figure captions

Fig. 1. One-body quasi-molecular shape sequence.

Fig. 2. Fission barrier of a ^{230}Th nucleus emitting a doubly magic ^{132}Sn nucleus. The dotted and dashed lines correspond to the macroscopic energy within the two-sphere approximation and the ellipsoidal deformations for the two-body shapes. The solid line includes the microscopic corrections.

Fig. 3. Cold fusion barriers versus the mass-centre distance r for the ^{70}Zn and ^{86}Kr on ^{208}Pb reactions.

Fig. 4. Warm fusion barriers versus the mass-centre distance r for the ^{48}Ca on ^{238}U and ^{248}Cm reactions.

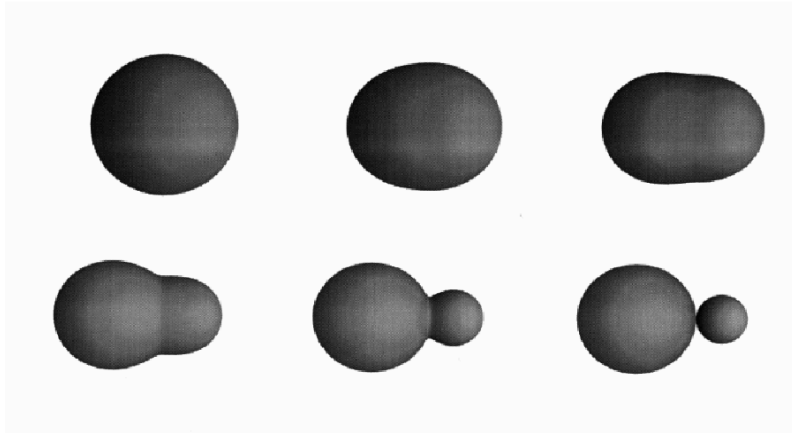


Figure 1 (G. Royer)

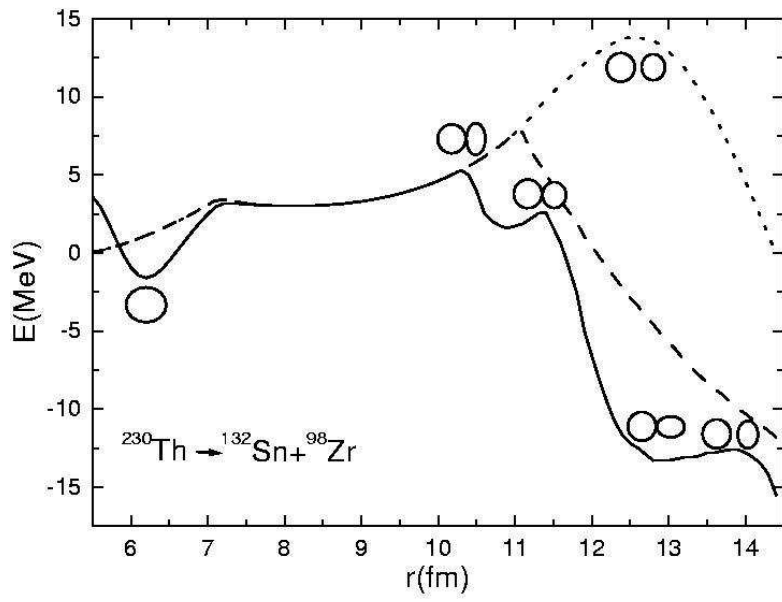


Figure 2 (G. Royer)

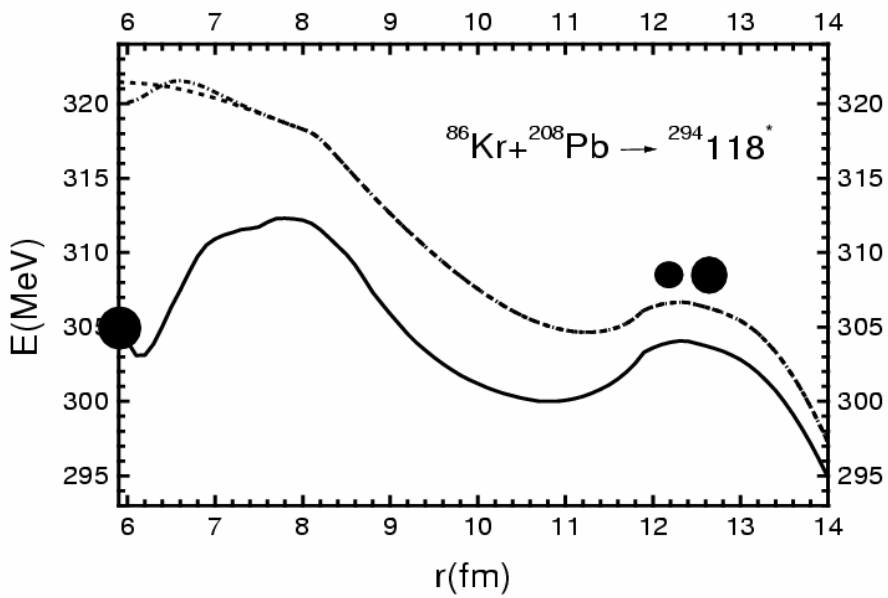
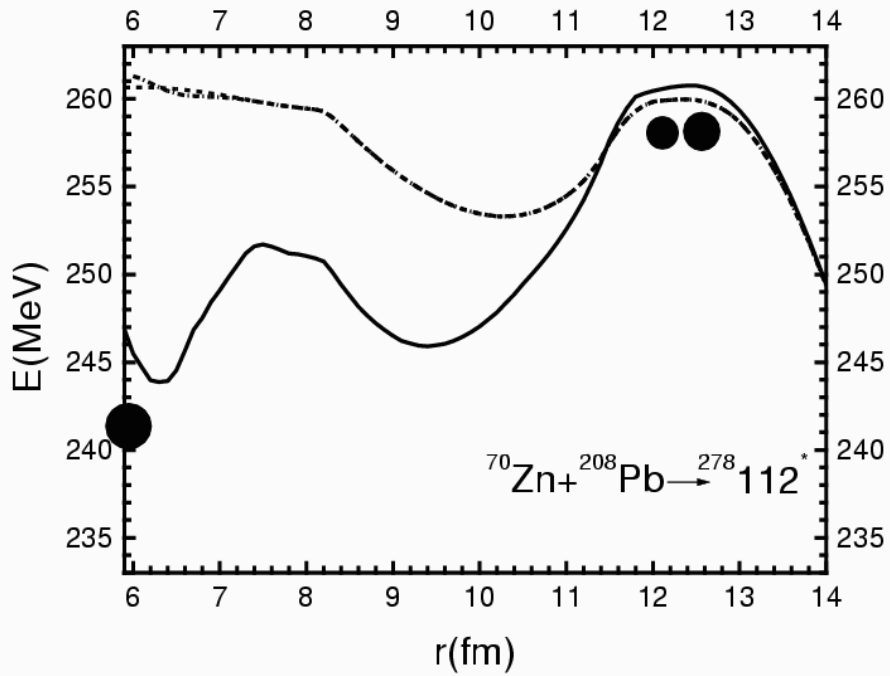


Figure 3

(G. Royer)

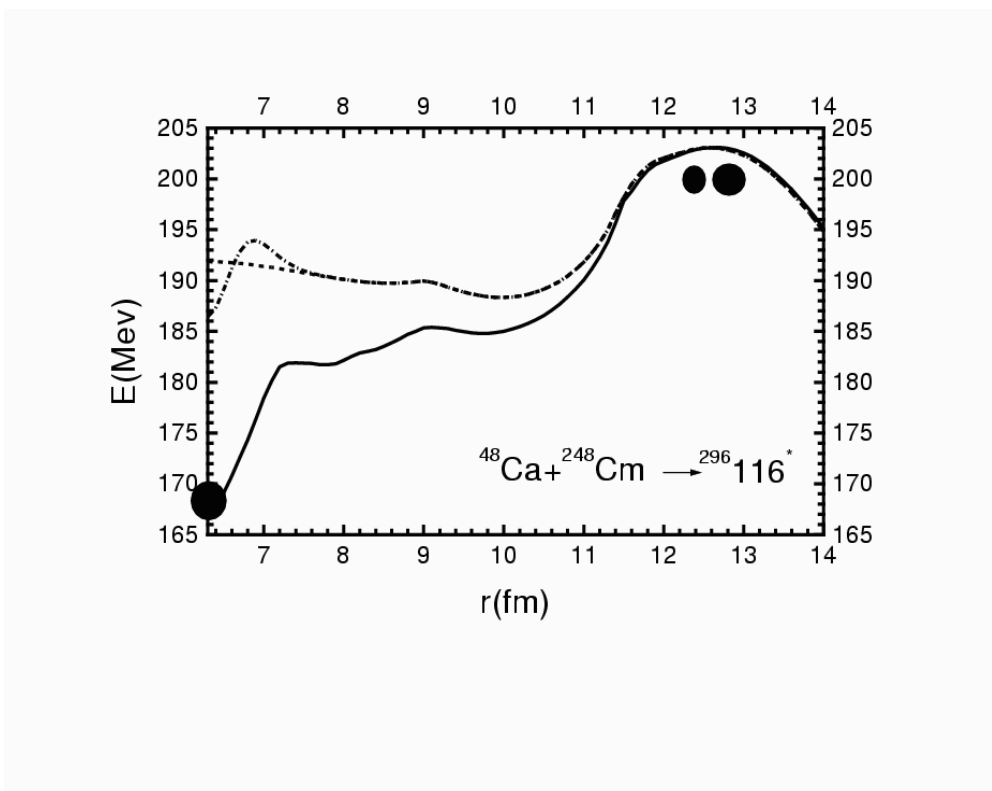
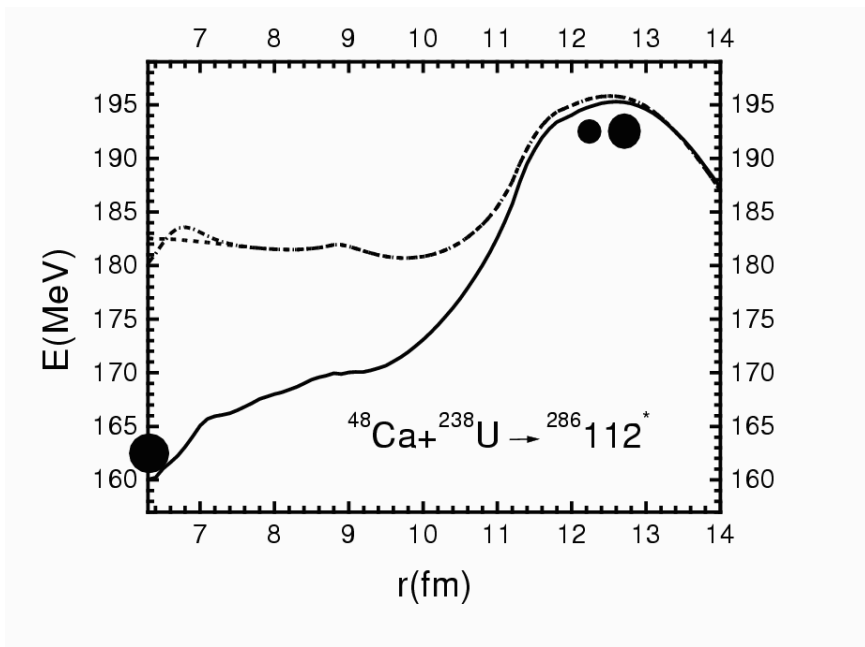


Figure 4

(G. Royer)